6 Particle Acceleration Experiments

In the previous chapters the phenomenon of electron acceleration was presented as a crucial process in the generation of X-rays based on laser-produced plasma. While Chapter 2 gave some insights into the theoretical background, in Chapter 4 several experiments on this topic were already reported. In this chapter, some additional experiments are described which elucidate properties of the accelerated electrons. For this purpose forward directed and collimated hot electrons were detected using a radiochromic film.
During the electron acceleration experiment, a strong emission of blue and green light was observed. The nature of this radiation will be discussed, since it gives interesting information on the plasma parameters. Finally, results from proton acceleration experiments will be presented.

6.1 Electron Acceleration

6.1.1 Target and Experimental Setup

In section 4.3 the absorption of hot electrons in different targets was discussed. While the focus there was on generation of bremsstrahlung, one might exploit the discussion for the planning of pure electron acceleration experiments as well. Fig. 4-14 shows the electron stopping ranges in water, gallium and gold. From this figure it is obvious that water is the preferred target for an investigation of electron acceleration, since most of the electrons will be transmitted from the laser focal region through the cold target material. For the acceleration of energetic protons, the same argument holds, since the electrons also have to cross the target, if the rear-side electron sheath is assumed to be the main source of accelerating forces (see section 2.5 for ion-acceleration mechanisms).
The experimental setup (Fig. 6-1) in the acceleration experiments did not differ much from that of the X-ray experiments. Essentially, the radiochromic film (40 mm behind the laser focus) and a large shutter were added to the setup. The system was aligned to produce a maximum level of ionizing radiation outside the chamber using the dose-rate meter TOL/F (Berthold Technologies [TOL]).

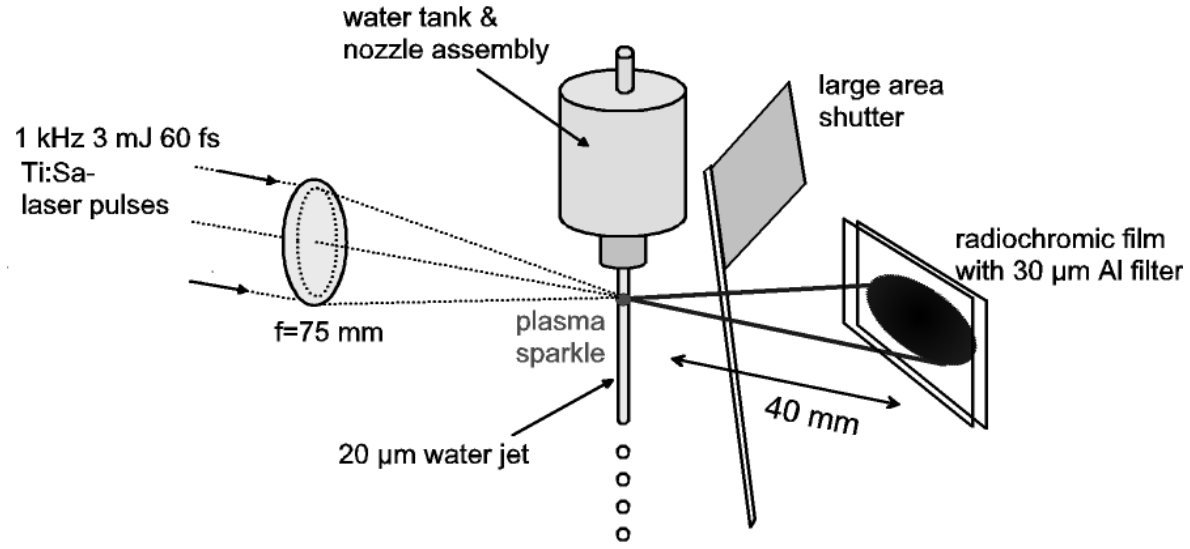

Fig. 6-1 : Experimental setup for the direct electron measurement.

6.1.2 Direct Electron Detection

There is a number of well-known methods for the detection of energetic electrons [SAN01]. Energetic means here a range of 50 to 500 keV and more, where the use of a semiconductor-spectrometer described in Chapter 4 is very limited. A traditional choice is the use of a magnetic electron spectrometer [MM96]. The energy resolution of such devices is quite good, but the spatial distribution is not resolved. Scintillation screens offer a good spatial resolution, but lack the energy information. Another (more indirect) class of methods is the use of in-target effects such as X-ray fluorescence and therefore a detailed examination of the line spectra (see section 2.3 for a discussion) and the broadband spectra. In our case such methods were used to determine the temperature of the hot electrons in different plasmas by their bremsstrahlung spectra (section 4.3). In the case of solid targets, the quantity of plasma-information derived from these methods can be increased by the use of layered or compound targets [EPF00]. For high electron energies above 10 MeV, photo-nuclear methods as presented in the work of Santala [SAN01] should be considered.

The method chosen for the experiments presented in this work is the detection with a combination of filter and electron-sensitive film. The (so called *radiochromic*) film used here is a GAFCHROMIC HD810 (Nuclear Associates [NA02]) covered with a 30 µm aluminum foil. When the active component in the radiochromic film (RCF) is exposed to ionizing radiation, it reacts to form a blue colored polymer with absorption maxima at about 615nm and 675nm. Further development is not necessary. Details of the film composition and its properties are given in Appendix C or at the companies web-site [NA02]. The calculated

stopping power for electrons in a 30 µm aluminum foil is about 60 keV [NIST02], therefore all recorded effects can be assumed to result from electrons of higher energy.

The laser energy applied in these experiments was determined to 2.7±0.1 mJ and the pulse length was 60 fs. In a first experiment (results shown in Fig. 6-2) the jet diameter was varied from 10 µm to 50 µm for an exposure time of 400 s (except for d=50 µm: 600s).

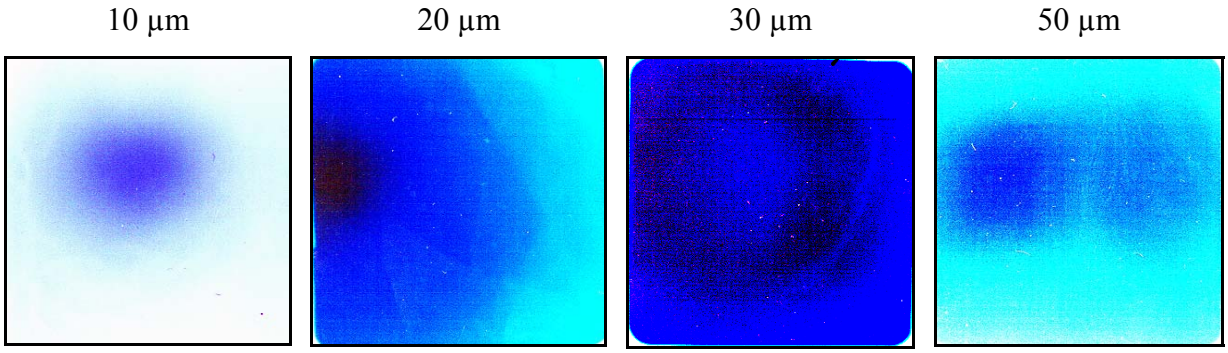

Fig. 6-2 : Colored RCF- scans for different jet diameter. The original film size is 50×50 mm.

A second test was carried out to prove the nature of the measured ionizing radiation since the reaction of the film is similar to gamma as well as to beta radiation. For this purpose a small magnet (12.7×12.7×3.2 mm, B = 0.2 T[1], NdFeB-magnet, Edmund Scientific) was fixed on the left side of the film (on top of the film holder). The result (Fig. 6-3) gives evidence that the detected radiation is entirely due to electrons, since the area close to the magnet is completely white. X-rays are apparently absent, since they would not be deflected by the magnet and the 30µm-aluminum foil is translucent for radiation of E > 6 keV. Protons can be excluded too, since the Al foil blocks all protons with less than about 2 MeV [NIST02]. From the test shown in Fig. 6-3 one can estimate the kinetic energy of the deflected electrons. Using the

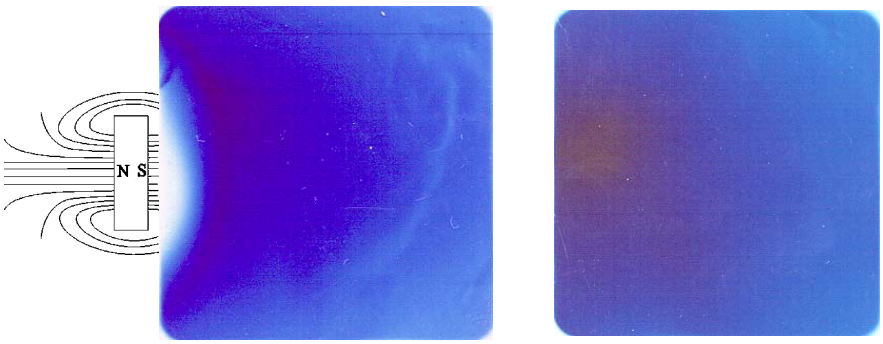

Fig. 6-3 : RCF with and without magnetic deflection of the detected electrons. On the left side the magnet with its field lines is sketched. In the experiment it sat directly on the left etch of the RCF.

[1] Measured with a LakeShore 450 Gaussmeter in 5 mm distance.

formula for the deflection Δx in a magnetic field (see e.g.[GKV89]):

$$\Delta x = \frac{qBl(l/2)}{mv} \quad , \qquad / \textbf{6-1}$$

where q is the elementary charge, B = 0.2 T is the magnetic field, l is the path length in the magnetic field and set equal to the physical extension of the magnet (12.7mm), m is the relativistic mass and v the velocity of the electron. Then the deflection of 10 mm corresponds to about 250 keV maximum electron energy. Since the magnetic field is far from being homogenous, this is only a rough approximation.

6.1.3 Discussion of Electron Energies

The results of more detailed investigations are presented in Table 6-1. In these experiments RCF was exposed to the electrons from water jets with diameters from 10 µm to 50 µm. The setup and laser settings are given in Fig. 6-1. The distance between laser focus and RCF was 40 mm and the exposed area on the RCF about 40 × 40 mm (which corresponds to a solid angle of 1 sr). The value of deposited energy dose was derived by converting the optical density of the film pieces into absorbed dose. The full procedure is described in detail in Appendix C. The deposited[1] electron energy E was calculated using the definition of the dose[2] D absorbed in a body of mass m: $D=E/m$. The active film layer has a volume V= 4cm × 4 cm × 6.5 µm and the density can be taken from water [NA02]. The (electron) energy per laser shot denotes the deposited energy divided by exposure time and repetition rate. The conversion efficiency is calculated from the energy of one laser pulse and the electron energy per laser shot.

For a deeper understanding of these numbers one might connect the electron energy data with the bremsstrahlung results presented in section 4.3 (in particular the broadband water

Table 6-1 : Electron-energy deposited in the RCF from different water-jet experiments.

Jet diameter d [µm]	Exposure time t_{ex} [s]	Deposited dose D [krad]	Total deposited electron energy E_{total} [J]	Deposited Energy E_{el} per laser shot [nJ]	Conversion efficiency E_{el}/E_{laser} [%]
10	400	7,83E+05	8,23E-05	0,21	1,03E-05
20	400	6,54E+06	6,87E-04	1,72	8,58E-05
30	400	9,95E+06	1,04E-03	2,61	1,31E-04
50	600	3,36E+06	3,53E-04	0,59	2,94E-05

[1] A calculation of the *emitted* electron energy (before, e.g., attenuation in the Al - filter) requires information on the energy distribution. It will probably lead to higher numbers.

[2] 1 krad ≈ 10 Gray = 10 J/kg, the use of non-SI unit krad is dictated by the manufacturers calibration data, see Appendix C.

spectrum in fig. 4-16 b). Although Fig. 4-16 suggest a limitation of the energy distribution at 50 or 60 keV, this is only a consequence of the low detector sensitivity. An extension of the spectrum to higher energies with decreasing flux can be supposed. And that is consistent with the results of the direct electron measurement: There, the overall-efficiency from total detected electron energy (per steradian and second, E>60 keV) to the incident laser energy is in the order of 10^{-4} % (Table 6-1). The energy of the broadband water spectra in Fig. 4-16 b) can be calculated (over all photons from 10 keV to 60 keV) to 0.05 mJ/s. This corresponds to a conversion efficiency of 1.6×10^{-3} %. Thus, the model with an energy distribution of the electrons centered at about 60 keV and a long slope towards higher energies supports both results. This is again illustrated in by the number of 60 keV electrons in Table 6-2 (assuming all exposure on the RCF would be due to monochromatic electrons) which is more than one order smaller than the numbers shown in Fig. 4-16.

6.1.4 Spatial Electron Distribution

Fig. 6-2 gives a first idea of the spatial distribution of the electron pattern on the RCF. A more detailed picture gives Fig. 6-4, where the data processed from the RCF-scans are shown. The procedure described in Appendix C was applied to convert the scanned data into a distribution of absorbed dose in units of krad. The full area corresponds to 1 sr or an angle of about 50 degree in vertical as well as in horizontal direction. Although interesting for a general understanding of the underlying processes, the distributions in the images c) and d) are probably not well suited for other experimental applications. The angular spread of the electrons is comparable in the images a) and b), but one should note that the maximum amplitude is ten times lower for the 10 µm jet. Further evaluation of Fig. 6-4 b) shows that 19% of the energy were deposited within an angle of 0.1 sr and 67% within 0.5 sr, respectively. Within a solid angle of more than 0.1 sr the average dose is larger than 100 krad or 1000 Gray in 400 seconds. This corresponds to more than 2.5 Gy/s irradiated into a cone of 17° by 24° full angle which has severe implications on laboratory safety precautions.

Taking the conversion numbers from Table 6-1 and the distribution images shown in Fig. 6-4, one can draw a number of conclusions about the influence of the jet diameter on the electron emission. The conversion efficiency is lowest for the 10 µm jet. In this case no green radiation (which will be discussed as an indicator for a wave-like acceleration process (section 2.4.2) later) was observed. Therefore one may assume that the target was fully evaporated in the focal region and the electron density was to small for efficient acceleration processes.

The emission angle increases up to d = 30 µm together with a growing conversion efficiency.

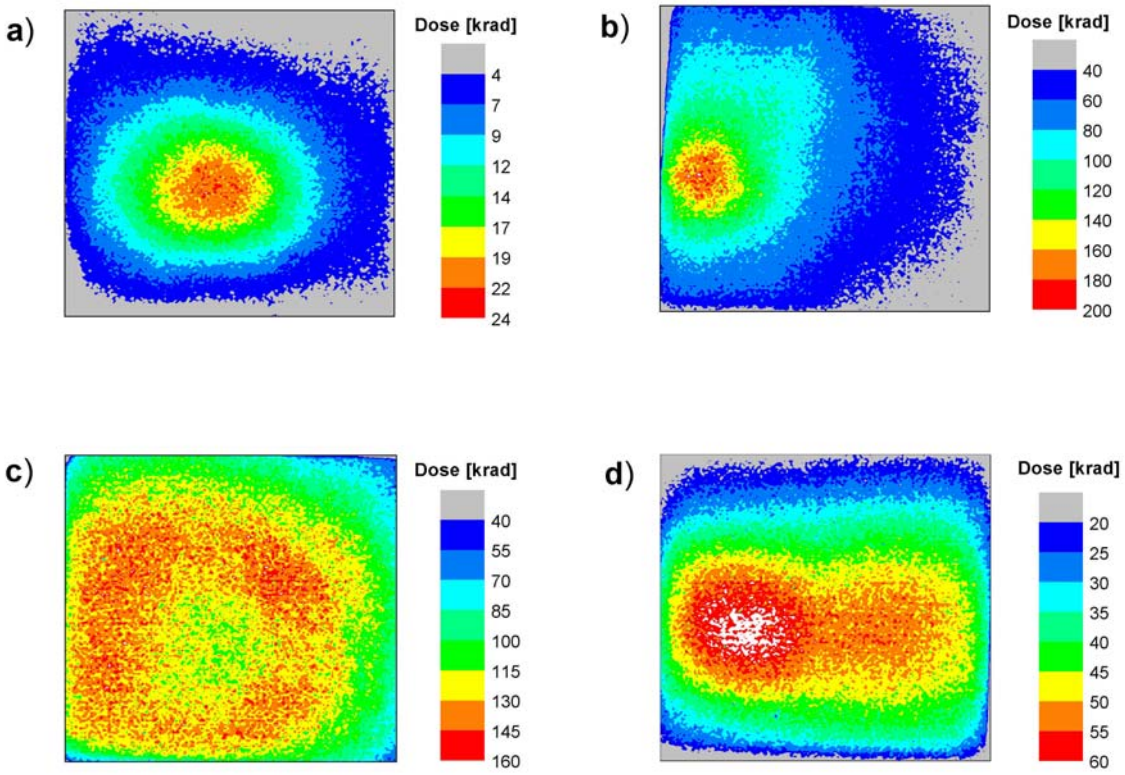

Fig. 6-4 : Electron-beam images recorded on RCF and converted to a contour plot of absorbed dose. The full area corresponds to 50°×50° equivalent to ~1sr. Water-target diameter and exposure time were a) 10 µm and 400 s, b) 20 µm and 400 s, c) 30 µm and 400s, d) 50 µm and 600s.

The effect (two spots) in the 50µm-case cannot to be explained with the simple diagnostics applied here; it might be due to increased absorption along the beam axis or cycling effects [MSP02]. From these graphs and the numbers in Table 6-2 it can be concluded that 20 µm is the best target diameter for the efficient generation of a directed beam of energetic electrons. Of course, this may change for stronger laser pulses.

Table 6-2 : Calculated electron numbers and charge transport figures for different target diameters.

Jet diameter d [µm]	Electron energy per shot E_{el} [J]	Number of 60 keV electrons[1] per shot Q_{pulse}/e	Average current[1] I in Coulomb/sec [A]	Peak current[1] in 50 fs $I_{max} = Q/\tau$ [mA]
10	2,06E-10	2,14E+04	3,42E-12	68
20	1,72E-09	1,79E+05	2,86E-11	572
30	2,61E-09	2,72E+05	4,35E-11	869
50	5,88E-10	6,12E+04	9,79E-12	196

[1] This assumes mono-energetic electrons only. This is a strong simplification, but one can at least expect a maximum in the energy distribution for 60 keV and an exponential decrease to lower energies (Al-absorption) as well as to higher energies (Maxwellian energy distribution with kT<60 keV).

For a comparison with other published results, it should be noted that the electron acceleration was not optimized in the experiments presented here. There are many reports about accelerated electrons, a detailed one comes from the group of D. Umstadter [CKM99], [DU01]. There, electrons with more than 40 MeV in a directed beam were detected. The laser with 4 TW peak power was focused into a 750 μm He-jet. The number of electrons per laser pulse was found to be about 10^{10} within a divergence angle of 1° - 3° FWHM[1]. This points to a number of tendencies: With increasing laser power the laser-electron interaction becomes more efficient, the energy of the individual electron increases, the number of hot electrons grows and the emission angle shrinks. The number of generated hot electrons is comparable to the number of electrons in a bunch from the linear accelerator used by Schoenlein et al. [SLC96] for laser-electron interaction experiments. The electrons from LINACs or synchrotrons have typically higher energy (50 MeV in 10…15 ps bunches in the experiments mentioned above) but the laser-generated electron bunches are much shorter (on the order of the laser pulse) and offer superior synchronization between laser and electron pulses (for pump and probe experiments). These advantages together with the table-top size are shared by the setup presented her, too. Apparently, the number of electrons generated here (Table 6-2) is smaller than reported elsewhere from ultrastrong lasers, and for applications (such as Thomson scattering [CMU98], [SLC96]) the laser energy must be increased and the electron-acceleration process needs optimization. Then, the setup presented here could offer additional advantages by its high repetition rate (ultra-strong lasers offer up to 10 Hz, the electron accelerator in Berkeley [SLC96] only 2 Hz, synchrotrons (BESSY 2) in single-bunch mode 1.25 MHz).

6.1.5 Spectral Observations

In Chapter 4 a first discussion of alignment procedures was given. There, minimal transmission was identified as the best parameter for alignment of the gallium-jet target. For the electron-acceleration experiments other parameters were found to be superior. The first of them was the dose measured outside the vacuum chamber with an ionization chamber (TOL/F [TOL]). Beside the fast rise of the dose level, another phenomenon appears when the alignment is improved: Blue light is emitted backward from the plasma, opposite to the incident infrared laser radiation. The light originates in the plasma and propagates to the focusing lens where it becomes a parallel pencil of light. Part of it is reflected onto the table by the laser-periscope before the vacuum chamber (see Fig. 6-5, left part). Another part is transmitted by

[1] Comparable results with more than 10^{10} electrons with MeV energy were reported by Gahn et al. [GTP02].

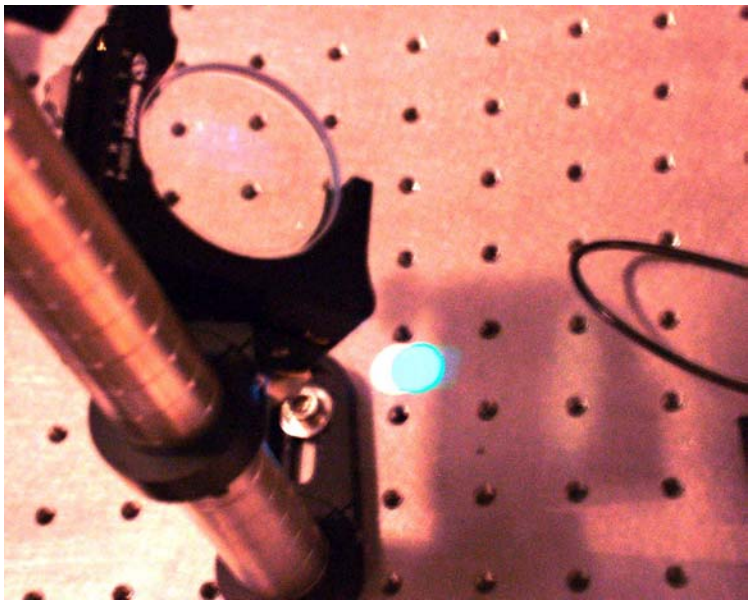

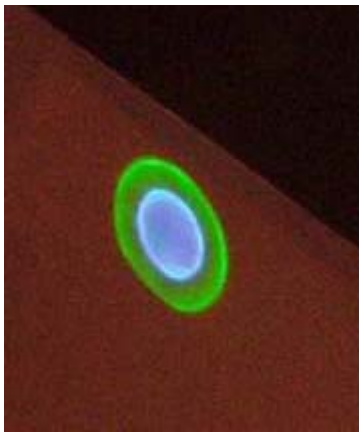

Fig. 6-5: Backward emitted light observed during electron-acceleration experiments.

the dielectric laser mirrors (optimized for 800 nm) and can be caught with white paper. By a further improvement of the alignment it was found, that at the point of maximum dose and maximum electron emission, a green circle appeared around the blue spot (Fig. 6-5, right part). While the blue light is a good indicator for alignment of the jet-position on a scale of 10…50 µm, the green appears only within a range of < 10µm around the position with maximum dose level. It should be mentioned, that the blue light was present in gallium experiments too, while the green ring appeared with water targets only.

The blue light was identified as the second harmonic of the laser light generated in the strongly non-linear regime in the laser focus. The green light was found to be the 3/2 harmonic of the incident laser light. 3/2 ω or (more general) odd-integer half-harmonic emission has been well known for a long time, e.g. from nanosecond laser experiments [SAB85], [RCD85] but also from femtosecond-laser produced plasma [AT02], [VTF02]. The processes for the conversion of the laser light into green backward-directed radiation are typical wave-like laser-plasma interactions as described in section 2.4. In particular, a two-plasmon decay (TPD) generates two electron-acoustic plasma waves at $\omega_{ea} \approx 0.5\ \omega_{laser}$. If the energy and the momentum conservation conditions are satisfied, such plasma waves are non-linearly mixed with reflected laser light (recombination) to form waves with a frequency of 3/2 the original laser frequency. As discussed in Chapter 2 this typically happens at quarter critical density (n_e=0.25 n_{crit}).

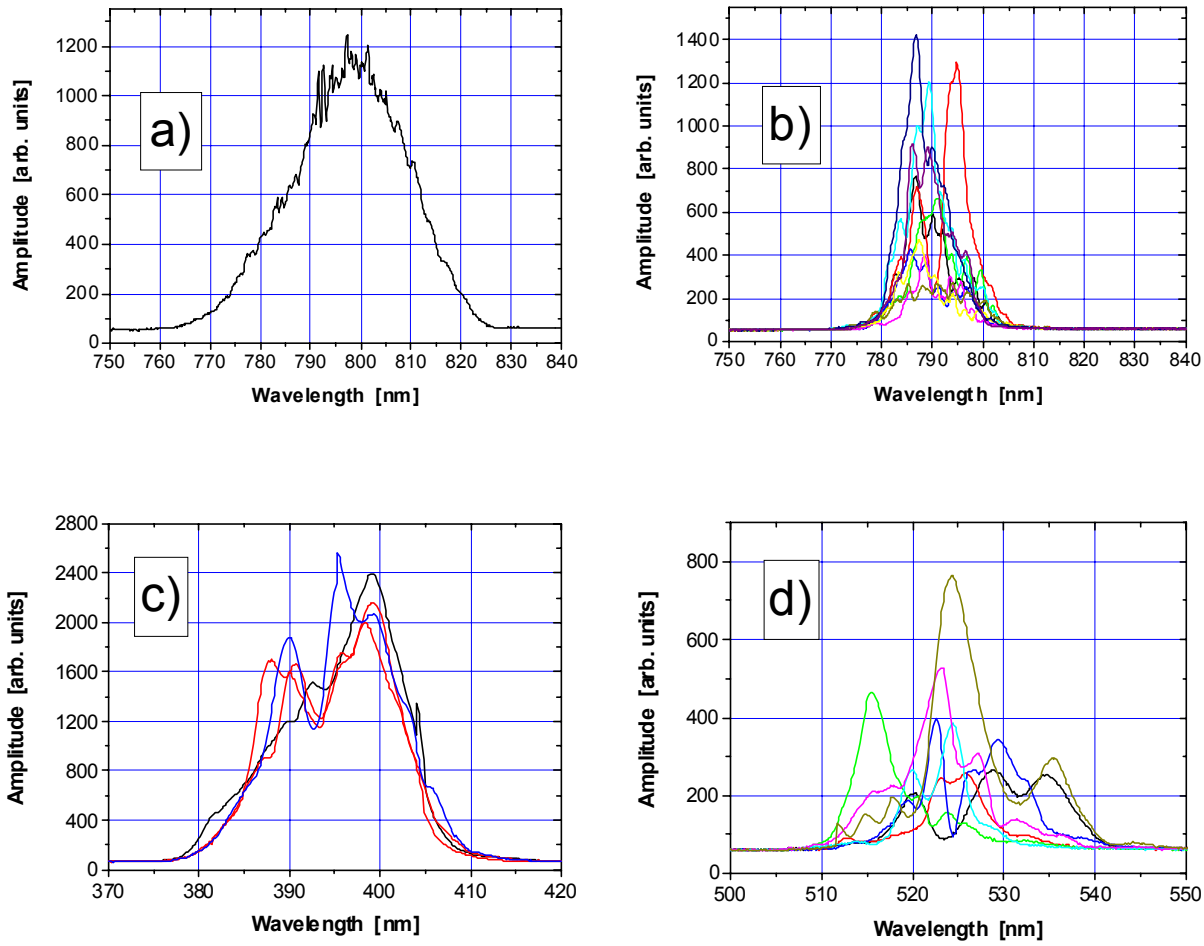

Fig. 6-6 : Spectral measurements during electron-acceleration experiments. a) Incident laser spectrum, b) backscattered IR light, c) backscattered blue light, and d) backscattered green light. The multiple curves demonstrate the statistical character of the spectra.

Since these laser-plasma interactions can easily be determined and the conditions of their growth are well known [DRA92], [HM79], one may draw some conclusions about the plasma. At first, the bare occurrence of the TPD tells something about the plasma: These processes need a low density gradient for efficient interaction, hence, one can presume (in fs-laser experiments) the presence of a prepulse with ps or ns distance to the main fs-laser pulse. Indeed, such a pulse (contrast about 1:500, distance 10 ns) was found with a fast photodiode (DET 210, Thorlabs, Inc.) as it was observed in other fs-laser experiments with 3ω/2 emission [VTF02]. Tarasevitch [AT02] even applied a delayed prepulse to investigate the influence of the prepulse. For a further investigation the back-scattered light was recorded during electron acceleration experiments[1] using a multi-band spectrometer (ORIEL 77400, grating 77411

[1] Laser: 2mJ, 50 fs; jet parameters: water, diameter 20 µm.

with 300 mm^{-1} from Oriel Instruments and a 24 bit CCD-sensor TH7802A from Thomson). Fig. 6-6 shows the results for the IR, the green and the blue spectral range, respectively. Exposure time was 100 ms, i.e. 100 pulses are collected within each curve. To visualize the remaining instability of the spectra, several curves are overlayed in each plot. The backscattered infrared radiation in Fig. 6-6 b) is due to laser light reflected on the critical surface in the plasma. Compared to the incident spectrum (Fig. 6-6a) one recognizes a general blue-shift of about 10 nm. This could be due to a Raman shift, but since a (more probable) red-shifted component is completely absent, Raman scattering seems highly improbable for this effect. Another interpretation seems more feasible: When the ultrashort laser-pulse is resonantly absorbed at the critical surface, the electrons are expelled with enormous velocities. Because of the thermal pressure the critical surface moves opposite to the laser pulse like a shock wave and the reflected light is Doppler shifted [LU92], [MU92]. Using $\Delta\lambda/\lambda = 2v/c$ the expansion velocity can be estimated to about 0.01c (=3×10^8 cm/s). A similar effect has been investigated at laser intensities of $10^{16}\ldots10^{18}$ W/cm² [KNS94]. The statistical character of this process accounts partially for the unstable behavior of the recorded spectra. An interaction of the reflected light with electron-acoustic waves, although not responsible for the general shift, might be another reason for the spectral scatter around 790 nm.

The blue spectra in Fig. 6-6c) show a double-peak structure with a separation of about 9 nm. Accordingly, this might be interpreted as the second harmonic of the laser light (399 nm) and a sum frequency (390 nm) generated from the Doppler-shifted and the unshifted component. A detailed description of the underlaying processes is difficult in this case since the bare spectral information does not allow to distinguish between photon-photon and photon-plasmon processes which both can contribute.

The green light at about 2/3 of the laser wave length is very unstable which was also reported from other experiments [VTF02], [SAB85]. The origin of this instable behavior may be connected to the statistical character of the involved plasma wave [AT02]. The center of the spectra is blue shifted to the actual value of 2/3 of the incident light. The dispersion diagram for the recombination process (fig. 2-8) explains this easily: Since the frequency ω_{pl} of the involved plasmon is slightly greater than the plasma frequency ω_p and the photon frequency at optimum conditions is slightly larger than $2\omega_p$ the resulting photon must be blue shifted. Although the green light could yield information on the plasma temperature, the instable character of this indicator made an exploitation difficult or impossible, even in extensive spectral investigations [SAB85] or with angular resolved observation [AT02].

Summarizing, it has been shown that spectral observation of plasma phenomena can yield valuable information on processes inside the plasma. In the experiments here the back-reflected light indicates a fast expansion of the critical electron-density surface. The direction of this movement should reverse at higher laser intensities when the light pressure balances the thermal pressure [LU92],[MU92],[KNS94]. The green light indicates wave-like electron-acceleration processes in an extended plasma. Beside that, it becomes apparent from these experiments that a detailed understanding of the complex plasma processes needs more and diverse measurements with, e.g., angular or temporal resolution.

6.2 Proton Acceleration

As reported by Gitomer et al. [GJB86], accelerated ions had been a observed regularly after high-power laser experiments became possible. While they represented an unwanted effect once, they are seen as an interesting means for several applications nowadays. These are, for instance, plasma diagnostics (Borghesi et al.[BSC01], [BBC02]) generation of radionuclides (Santala et al.[SZB00], Nemoto et al. [NMB01]), and photoneutrons (Pretzler et al. [PSP98], Disdier et al. [DGM99], Schwoerer et al.[SGD01]). The generation of radionuclides also includes positron emitters (Spencer et al. [SLS01], Roth et al. [RCB01], Perry et al. [PSC99], Santala [SAN01], Gahn et al.[GTP02]). Furthermore the use of energetic protons for fast ignition of nuclear fusion was suggested by Roth et al.[RCK01].

To test the capability of the water-jet apparatus for the generation of energetic protons (the dominant ion-species from a water target) a number of experiments were conducted. The experimental setup (see Fig. 6-7) was similar to that used for the direct detection of hot

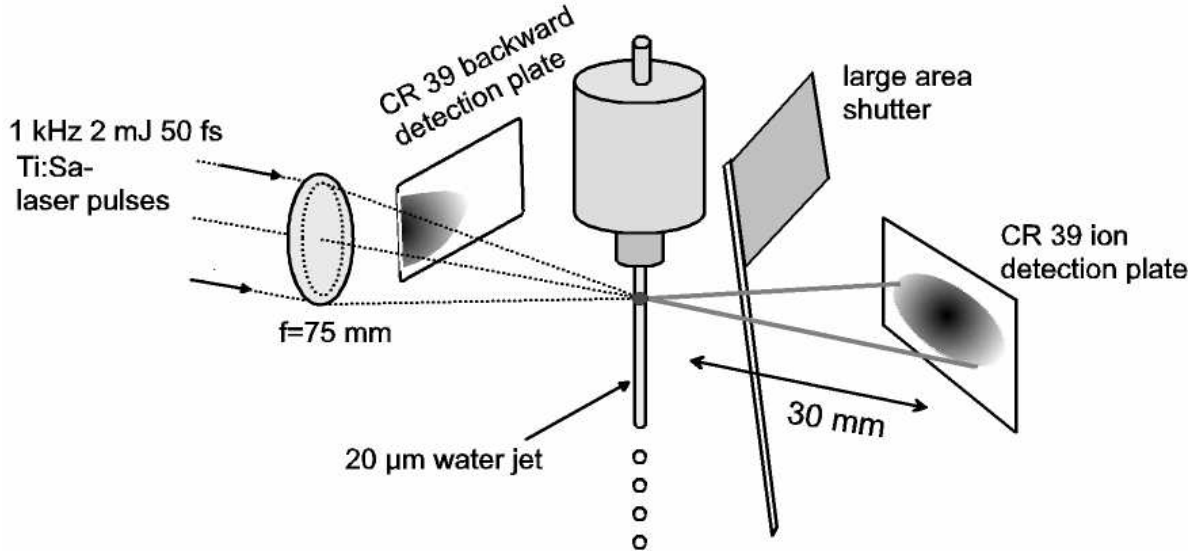

Fig. 6-7 : Schematic of proton acceleration and detection setup.

electrons. The detection material (CR39 or TASTRAK) is a clear plastic sensitive to charged ions of more than 100 keV kinetic energy. Details of the processing and the track-counting method are given in Appendix D.

6.2.1 Proton Energy

For the determination of the proton energy, several methods are well-known: detection by CR 39 (bare, stacked [MKS01], stacked with RCF [MSP02], with increasing absorbers [CKD00], with track analysis), magnetic or Thomson spectrometer (ions deflected in magnetic [MGF00] and electric field [HKP02], recorded with CR39 or RCF), nuclear activation effects (ion-induced nuclear reactions [SAN01], [HBC00]), Faraday cups (time resolved charge collection [GJB86]) and many others. References mentioned here are examples of applications, not the sources of the individual techniques.

For our proof-of-principle experiments we chose the simple method of detection in CR 39 with an increasing number of Mylar absorber foils on top (see, for instance, Nemoto et al. [NMB01]). The Mylar foil had a thickness of 1.8 µm. For the experiments the detector plates were covered with several layers of this foil. The energy range[1] of transmitted protons then can be calculated [NIST02] as follows:

Mylar layer	Mylar thickness	Proton energy threshold
None	–	E > 100 keV[2]
1 layer	1.8 µm	E > 250 keV
2 layer	3.6 µm	E > 350 keV
3 layer	5.4 µm	E > 430 keV

Proton experiments were conducted using laser pulses of 50 fs duration and 2 mJ energy at 1 kHz repetition rate. Results for jet diameter of 10 µm and 20 µm are shown in Table 6-3.

As expected from the previous electron acceleration experiments, the proton yield from the 10µm jet is smaller than from the 20µm jet. The total number of protons in the latter experiment (assuming isotropic emission) can be extrapolated to about 1000 per laser pulse.

Since in this experiment the CR39 was already overexposed, a separate run with only 10 s exposure time (jet diameter 20µm) was conducted leading to an extrapolation of about 3×10^3 protons (E > 100 keV) per laser shot. The maximum proton energy was determined to about 400 keV, since no tracks were found under 3 layers of Mylar.

[1] A threshold up-shift of about 10 keV due to attenuation in the water vapor in the chamber (p = 5 mbar) has been neglected.

[2] Lower limit of 100 keV is defined by the sensitivity threshold of CR39.

Table 6-3 : Results of proton acceleration experiments with different water-jet diameter.

	20 µm jet, 60 s exposure			10 µm jet, 300 s exposure		
MYLAR Cover[1]	Track density [mm^{-2}]	Tracks per second [$s^{-1}mm^{-2}$]	Tracks per second and solid angle [$s^{-1}sr^{-1}$]	Track density [mm^{-2}]	Tracks per second [$s^{-1}mm^{-2}$]	Tracks per second and solid angle [$s^{-1}sr^{-1}$]
none	146 000	2430	73 000	131 000	436	13 100
1 layer	6 200	104	3 100	15 700	52	1 570
2 layer	2 650	44	1 320	10 500	35	1 050

Backward-emitted protons were detected with a CR39 plate behind the target (see Fig. 6-7) covering an angular range of about 30…60° to the optical axis. The number of backward-emitted protons was comparable to that of the forward-directed protons, but no tracks were found under Mylar cover. This leads to the conclusion that protons are accelerated almost isotropic, but with higher energy-transfer efficiency in the forward direction. The aspect of spatial distribution will be discussed in more detail in the next sub-section.

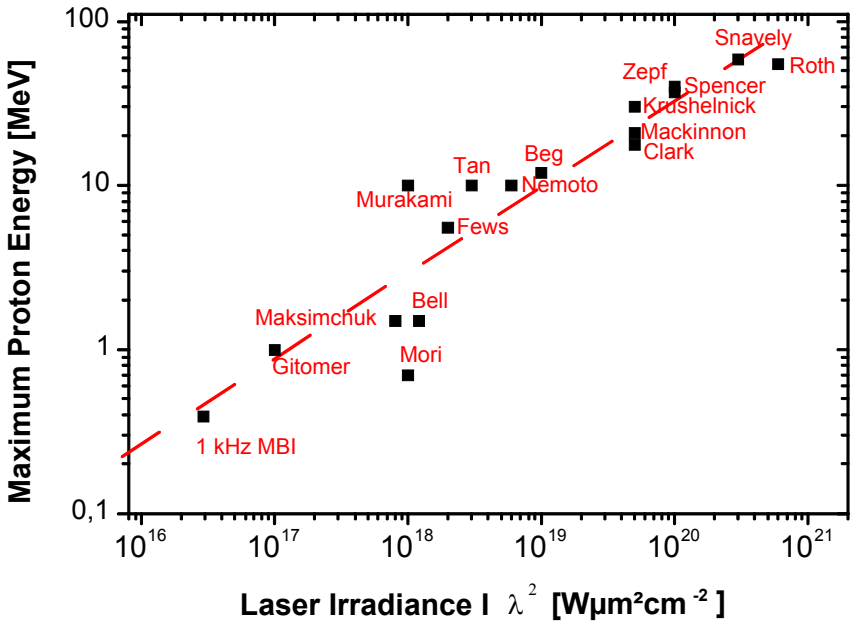

Fig. 6-8 : Maximum proton energy results from various laser systems. The names in the graph denote the respective first author of the following publications: Snavely et al. [SKH00], Roth et al.[RCB01], Zepf et al.[ZCK01], Spencer et al.[SLS01], Krushelnick et al.[KCZ00], Mackinnon et al.[MBH01], Clark et al.[CKD00], Beg et al.[BBD97], Nemoto et al.[NMB01], Tan et al.[TMW84], Muralkami et al.[MKS01], Fews et al.[FNB94], Bell et al.[BBC93], Maksimchuk et al.[MGF00], Mori et al.[MKK98], and Gitomer et al.[GJB86]. 1kHz MBI denotes the results from the first 1 kHz experiments presented in this work [TKR03].

[1] No tracks under 3 layers of MYLAR.

A comparison of the maximum proton energies from the water-jet experiments with results from various other laser systems is given in Fig. 6-8. The dashed line in the graph is a least-square linear fit through the numbers resulting in a general tendency for the maximum proton energy E_{max} depending on the laser irradiance $I\lambda^2$ as follows: $E_{\max} \propto \left(I\lambda^2\right)^{0.52}$. This is in good agreement with previous publications [GJB86], [CKZ00]. One can conclude from the graph: a) that the proton acceleration process does not depend on the type of target, and b) which proton energies can be expected for increased laser parameters. Furthermore one can also expect a remarkably higher laser-to-proton-energy conversion efficiency (e.g. a few percent at 2×10^{18} Wμm²/cm² [FNB94], [BBC93] compared to about 10^{-6} % in our experiments, where no effort had been made for proton yield optimization).

A comparison of the maximum electron and proton energies is difficult, since the maximum electron energy was not determined. The lower limit of electron energy was set to 70 keV due to Al-filter transmission, therefore an estimation of 100 keV for the maximum electron energy seems realistic. That would give a factor of 4 when compared to the maximum proton energy of about 400 keV, which agrees well with results of other experiments (factor 4.5 [GJB86]) or simulations (factor 4 [SBF02]). Furthermore it should be mentioned, that simulations [SBF02] with inclusion of a preplasma due to finite intensity contrast of the laser pulses predict the production of MeV protons at laser intensities $I > 5\times10^{17}$ W/cm². This should be obtainable in the near future.

6.2.2 Angular Distribution

In a setup as sketched in Fig. 6-7, the detector plates cover a solid angle of 1.8 sr corresponding to horizontal (vertical) full angles of about 65°. The plates were centered to the optical axis in forward direction and shifted by about 30° in the backward direction. In most of the experiments only a slow decrease in track density (maximum on the optical axis) has been observed. This is illustrated by the left image in Fig. 6-9. The detector plate shown there is overexposed which allows inspection by eye or, with some illumination difficulties, by photography. Except the structure in the center, the lower part is homogeneously whitened by proton tracks. Protons flying onto the upper part were blocked by the physical extension of the nozzle apparatus (laser focus about 1 mm underneath the orifice). It may be assumed from the geometry of the system that there is no difference in the upward proton emission compared to the downward emission. As mentioned above the track density in backward direction was not much different from that detected in forward direction, except for the

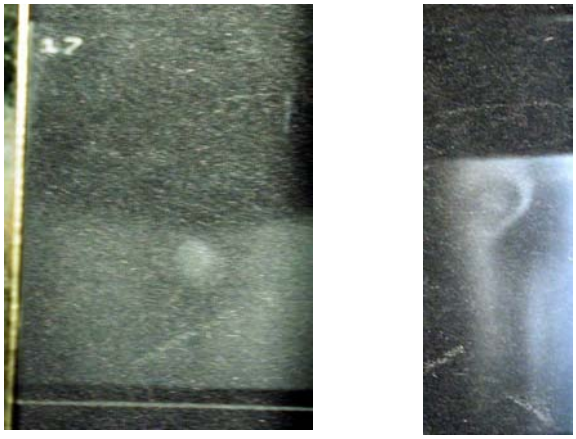

Fig. 6-9 : Photographed images of CR39 exposed to energetic protons showing isotropic distribution with circular features in the center.

absence of protons with $E > 250$ keV.

The circular structure in the center of both images in Fig. 6-9 was an unstable feature and appeared only in a few cases. The experimental settings for the images presented here were comparable:

- Left Image : 20 s exposure, 2 mJ laser pulse energy, 3 mbar chamber pressure
- Right Image : 30 s exposure, 2.4 mJ laser energy, 0.7 mbar chamber pressure.

In both cases water jets with a diameter of 20 µm were applied, laser pulse length and repetition rate were, 50 fs and 1 kHz, respectively. The full angle of the ring is about 12° in the left image and about 15° in the right one (corresponding to 0.05 sr and 0.07 sr). They are centered around the laser axis.

Such ring structures are well known from experiments with higher laser irradiances and planar targets. Zepf et al. [ZCK01] found that each ring contains protons of a certain energy level and that the proton energy increases with decreasing ring-diameter. Furthermore, they reproduced this effect with a number of different targets. This underlines again that proton acceleration might be due to processes that are almost independent of the target material. A quantitative analysis of the emission angles as suggested by Murakami et al. [MKS01] could give information on the acceleration processes inside and behind the target, in particular on the structure of the magnetic fields. But this requires a massive theoretical support as well as a stable and reproducible effect. The latter should be attainable with an increase of laser power. Then one should find proton energies in the MeV range.

Finally, one point in the qualitative picture of the directed protons from a microscopic water-jet target should be mentioned: With the model of *target normal sheath acceleration* (TNSA) as suggested by Wilks et al. [WLC01] protons are generally accelerated normal to the rear surface of the target by an *electron sheath*. It was suggested by different groups [WLC01], [BEC00] to form targets with a concave rear surface to obtain a focusing effect in the proton beam. The effect of a directed proton beam from a *convex* target[1] as seen in our experiments contradicts this idea. An explanation of this phenomenon could be connected to the distribution of the hot electrons as presented in previous sections of this chapter. Furthermore, effects on the CR 39 due to hot electrons or x-rays cannot be explicitly excluded, although they appear not very probable if one takes the short illumination time into account (20 times shorter than in the direct electron measurements presented in table 6-1).

In any case more experimental and theoretical work beyond the experiments presented here is needed for a full understanding of this problem, which then could be a valuable part of the ongoing discussion about the acceleration processes for energetic ions in laser plasmas.

[1] Roth et al. [RCG01] produced a horizontal stripe of protons on CR39 from a thin vertical wire target (in agreement with the TNSA model). A horizontal stripe was not apparent in any of the experiments with the water jet.